Metabolism and Bioenergetics:

Identification of Hydrogen Bonds to the Rieske Cluster through the Weakly Coupled Nitrogens Detected by Electron Spin Echo Envelope Modulation Spectroscopy

Sergei A. Dikanov, Derrick R. J. Kolling, Burkhard Endeward, Rimma I. Samoilova, Thomas F. Prisner, Satish K. Nair and Antony R. Crofts

J. Biol. Chem. 2006, 281:27416-27425.
doi: 10.1074/jbc.M604103200 originally published online July 19, 2006

Access the most updated version of this article at doi: 10.1074/jbc.M604103200

Find articles, minireviews, Reflections and Classics on similar topics on the JBC Affinity Sites.

Alerts:
- When this article is cited
- When a correction for this article is posted

Click here to choose from all of JBC's e-mail alerts

This article cites 54 references, 2 of which can be accessed free at
http://www.jbc.org/content/281/37/27416.full.html#ref-list-1

Downloaded from http://www.jbc.org/ at Frankfurt University Library / Section Bibliothek Naturwissenschaften on November 8, 2013

THE JOURNAL OF BIOLOGICAL CHEMISTRY VOL. 281, NO. 37, pp. 27416–27425, September 15, 2006
© 2006 by The American Society for Biochemistry and Molecular Biology, Inc. Printed in the U.S.A.

Identification of Hydrogen Bonds to the Rieske Cluster through the Weakly Coupled Nitrogens Detected by Electron Spin Echo Envelope Modulation Spectroscopy*

Received for publication, April 28, 2006, and in revised form, July 7, 2006 Published, JBC Papers in Press, July 19, 2006, DOI 10.1074/jbc.M604103200

Sergei A. Dikanov[‡1], Derrick R. J. Kolling[§2], Burkhard Endeward[¶], Rimma I. Samoilova[‖], Thomas F. Prisner[¶], Satish K. Nair[§], and Antony R. Crofts[§**3]**

*From the [‡]Department of Veterinary Clinical Medicine, University of Illinois, Urbana, Illinois 61801, the [§]Center for Biophysics and Computational Biology, University of Illinois, Urbana, Illinois 61801, the [¶]J. W. Goethe Universität, Institut für Physikalische und Theoretische Chemie, D-60438 Frankfurt, Germany, the [‖]Institute of Chemical Kinetics and Combustion, Russian Academy of Sciences, Novosibirsk 630090, Russia, and the **Department of Biochemistry, University of Illinois, Urbana, Illinois 61801*

The interaction of the reduced [2Fe-2S] cluster of isolated Rieske fragment from the bc_1 complex of *Rhodobacter sphaeroides* with nitrogens (^{14}N and ^{15}N) from the local protein environment has been studied by X- and S-band pulsed EPR spectroscopy. The two-dimensional electron spin echo envelope modulation spectra of uniformly ^{15}N-labeled protein show two well resolved cross-peaks with weak couplings of ~0.3–0.4 and 1.1 MHz in addition to couplings in the range of 6–8 MHz from two coordinating N_δ of histidine ligands. The quadrupole coupling constants for weakly coupled nitrogens determined from S-band electron spin echo envelope modulation spectra identify them as N_ϵ of histidine ligands and peptide nitrogen (N_p), respectively. Analysis of the line intensities in orientation-selected S-band spectra indicated that N_p is the backbone N-atom of Leu-132 residue. The hyperfine couplings from N_ϵ and N_p demonstrate the predominantly isotropic character resulting from the transfer of unpaired spin density onto the 2*s* orbitals of the nitrogens. Spectra also show that other peptide nitrogens in the protein environment must carry a 5–10 times smaller amount of spin density than the N_p of Leu-132 residue. The appearance of the excess unpaired spin density on the N_p of Leu-132 residue indicates its involvement in hydrogen bond formation with the bridging sulfur of the Rieske cluster. The configuration of the hydrogen bond therefore provides a preferred path for spin density transfer. Observation of similar splittings in the ^{15}N spectra of other Rieske-type proteins and [2Fe-2S] ferredoxins suggests that a hydrogen bond between the bridging sulfur and peptide nitrogen is a common structural feature of [2Fe-2S] clusters.

Proteins containing Rieske-type [2Fe-2S] clusters with two histidyl and two cysteinyl ligands play important roles in many biological electron transfer reactions such as aerobic respiration, photosynthesis, and biodegradation of various alkene and aromatic compounds. The distinct biological functions of this protein family are in part associated with the cluster redox potential and the p*K* of the oxidized form, which are roughly correlated with the number of hydrogen bonds from protein side chains and the peptide backbone to the cluster and its immediate ligands (1–6).

In the cytochrome bc_1/b_{6f} family, a Rieske iron-sulfur protein (ISP)[4] is a constituent of the high potential electron transfer chain that accepts the first electron in the bifurcated reaction at the ubihydroquinone (quinol, QH_2) oxidizing Q_o site. In the catalytic mechanism at the Q_o site, the redox reaction involves extraction of both an electron and a proton from the bound quinol and their transfer to the ISP through a short pathway that includes the ISP His-161 ring and the H-bond between N_ϵ and the -OH of the quinol substrate (7). It has been proposed that the electron transfer is gated by the low probability of finding the H-atom of the H-bond in the kinetically favorable position, determined by the p*K* difference between the quinol and the oxidized ISP (ISP_{ox}) (reviewed in Refs. 5 and 6). The p*K* on ISP_{ox} is contributed by one of the cluster ligands, His-161 in bovine numbering, and is associated with H^+ dissociation from the N_ϵ involved in the H-bond. The gating accounts for the fact that this first electron transfer is slower by more than 3 orders of magnitude than would be expected from the short distance (~7 Å) involved (6, 7). The first electron transfer is the rate-determining step in quinol oxidation under conditions of substrate saturation. Rate determination at this reaction is demonstrated by the fact that the overall rate depends on its driving force in a classical Marcus fashion, as shown through use of mutants of the ISP with modified redox potential (6–13). Briefly, the driving force, ΔG^o, for the first electron transfer is determined by the redox potential difference between the donor (SQ/QH_2) and acceptor (ISP_{ox}/ISPH) couples. Assuming that mutations in the ISP do not change $E_m(SQ/QH_2)$, a change in

* This work was supported by National Institutes of Health Grants GM 35438 (to A. R. C.) and GM 62954 (to S. A. D.), Fogarty Grant PHS 1 RO3 TW 01495 (to A. R. C. and R. I. S.), and National Institutes of Health/National Center for Research Resources Grant S10-RR15878 for instrumentation. The costs of publication of this article were defrayed in part by the payment of page charges. This article must therefore be hereby marked "*advertisement*" in accordance with 18 U.S.C. Section 1734 solely to indicate this fact.

[1] To whom correspondence may be addressed. E-mail: dikanov@uiuc.edu.
[2] Present address: Dept. of Chemistry, Princeton University, Princeton, NJ 08540.
[3] To whom correspondence may be addressed. E-mail: a-crofts@life.uiuc.edu.

[4] The abbreviations used are: ISP, Rieske iron-sulfur protein; ESEEM, electron spin echo envelope modulation; ISF, the water soluble proteolyzed extrinsic domain of the Rieske subunit (the iron-sulfur fragment) of the bc_1 complex from *R. sphaeroides*; HYSCORE, hyperfine sublevel correlation; NQR, nuclear quadrupole resonance; N_p, peptide nitrogen; MOPS, 4-morpholinepropanesulfonic acid; mT, millitesla.

E_m (ISP_{ox}/ISPH) will effect the driving force. Marcus theory relates the rate constant to the driving force, and a plot of $\log_{10}k$ v. ΔG^o follows the expected form for rates measured in mutants generated in mitochondria or in different species of bacteria (6, 7, 13). Because the oxidation of QH_2 is the limiting partial process and the Marcus limitation is seen for the first but not the second electron transfer step, the location of the limiting step is unambiguous (6, 7). It is clear, therefore, that, for this crucial reaction, a deeper analysis of the factors contributing to changes in E_m of ISP, and in the pK_a values of the N_ϵ, will play a key role in our understanding of the overall mechanism (5–7).

An informative approach to studying the environment of the reduced Rieske cluster is through application of high resolution EPR techniques. Indeed, the coordination of the Rieske cluster by histidyl ligands was initially established by electron nuclear double resonance spectroscopy (14–16) and confirmed by ESEEM (17, 18) before being demonstrated through crystallography (19). Further studies of the Rieske cluster by X-band one- and two-dimensional ESEEM (20–22) have shown that the major contribution in these spectra comes from the coordinating N_δ of histidines. Other more weakly coupled ^{14}N nitrogens present in the cluster environment do not produce recognizable lines in the spectra, because of the influence of the nuclear quadrupole interaction of ^{14}N. Whether or not lines are seen depends on a particular relation between nuclear Zeeman frequency and hyperfine coupling (23, 24), as explained under "Experimental Procedures." Recently, it was demonstrated that the weakly coupled nitrogens produce readily observed lines in X-band two-dimensional ESEEM (HYSCORE) spectra of ^{15}N-labeled sulredoxin, another Rieske-like protein (25). In particular, two weak couplings of ~0.7 and 0.25 MHz (where the values reflect a recalculation of frequencies for comparison with ^{14}N) were observed and tentatively assigned to peptide nitrogen of the backbone, and to N_ϵ of the histidine ligands, respectively, based on comparison with model complexes and other clusters (25). However, these data did not provide any direct indication for the chemical nature of the nitrogens producing the couplings observed.

This finding is important in the context of functional studies of the bc_1/b_{6f} family because it opens the way for the spectroscopic characterization of the N_ϵ nitrogen involved in H-bonding with the occupant of the Q_o site and the nitrogen(s) N_p forming H-bonds with the cluster.

In the present article, we have applied X-band (~9.7 GHz) and S-band (~3.1 GHz) spectroscopy to the water soluble proteolyzed extrinsic domain of the Rieske subunit (the iron-sulfur fragment (ISF)) of the bc_1 complex from *Rhodobacter sphaeroides* to further study the weakly coupled nitrogens around the Rieske cluster.

EXPERIMENTAL PROCEDURES

Sample Preparation—Growth of *R. sphaeroides*, purification of the bc_1 complex, and isolation of the ISF were previously described (26–28).

Protein isotopically labeled with ^{15}N was prepared from *R. sphaeroides* grown in Sistrom medium as described previously (26), but with the following modifications: 50% less nitrilotriacetic acid was used, L-aspartate and L-glutamate were not used, and ^{15}N ammonium sulfate (Aldrich) replaced ^{14}N ammonium sulfate. The working buffer used for all of the ISF samples was 50 mM KH_2PO_4, pH 7.0, 400 mM NaCl, and 20% (v/v) glycerol. The samples were reduced with 5 mM buffered (50 mM MOPS, pH 7.0) sodium ascorbate and placed into a quartz cuvette (Wilmad-Labglass, Bueno, NJ) with Teflon tubing to prevent scratching. In all of the spectra reported in this paper, the ISF was used rather than the intact complex. As a consequence, no interactions between the ISP extrinsic domain and occupants of the Q_o site could occur, and the spectra therefore lack the features associated with such interactions.

Pulsed EPR Spectroscopy—In pulsed EPR, a magnetization vector, reflecting a population of electron spins aligned along the magnetic field, is rotated to a new alignment, and the kinetics of relaxation back to the equilibrium alignment is followed by detecting the microwave emission (the echo). The rotation of the magnetization is determined by the pulse length, 90° for a $\pi/2$ pulse, 180° for a π pulse. The interaction with nuclear spins results in modulation of the decay kinetics, and Fourier transformation of these modulations reveals the frequencies of the interacting species. In practice, the resolution is improved through use of ESEEM (see below). For the Rieske protein in frozen solution, different orientations of the cluster relative to the magnetic field vector can be selected by tuning the magnetic field within the anisotropic EPR line from the rhombic g-tensor. The orientation of the g-tensor axes is strictly connected with the cluster.

Several types of electron spin echo measurements with different pulse sequences were used, with appropriate phase cycling schemes employed to eliminate unwanted features from experimental echo envelopes (29, 30). Among them were two-pulse sequence and one- and two-dimensional three- and four-pulse sequences (29–31).

Two-pulse Field Sweep—In experiments using the two-pulse sequence ($\pi/2$ - τ - π - τ - echo), the intensity of the echo signal was measured with a fixed interval, τ, between two microwave pulses with spin vector rotation angles $\pi/2$ and π. The echo intensity varies with magnetic field strength (units mT) to show the spectrum of the absorbing species. This type of measurement is termed a "field sweep," and at settings at which modulation from magnetic nuclei are minimized (long pulse lengths, $\pi \geq 100$ ns), the EPR line is comparable with the integral of the derivative spectrum collected by continuous wave-EPR.

One-dimensional Three-pulse ESEEM—In ESEEM spectroscopy, the spin echo envelope, resulting from measurement of changes in amplitude of the echo with variation of pulse timing, provides an averaging of the relaxation kinetics of the spin population, improving resolution. In the one-dimensional three-pulse measurement ($\pi/2$ - τ - $\pi/2$ - T - $\pi/2$ - τ - echo), the intensity of the stimulated echo signal after the third pulse is recorded as a function of time, T, at constant time, τ, to generate an echo envelope. The set of three-pulse envelopes recorded at different τ values forms, after Fourier transformation, a two-dimensional three-pulse data set showing the spectra caused by nuclear spins interacting with the paramagnetic center (29–31).

HYSCORE—In the two-dimensional four-pulse experiment ($\pi/2$ - τ - $\pi/2$ - t_1 - π - t_2 - $\pi/2$ - τ-echo) known as HYSCORE, the

intensity of the inverted echo after the fourth pulse was measured with varied t_1 and t_2 and constant τ (30). Such a two-dimensional set of echo envelopes gives, after Fourier transformation, a four-quadrant spectrum that selects different correlations between nuclear frequencies from two manifolds with opposite electron spin projections, with equal resolution in each frequency coordinate. Because the spectrum is symmetrical with respect to the zero axes, only two quadrants are usually shown (30). The data are usually presented as contour plots to show the peak positions in the spectra arising from different nuclear spin interactions or as three-dimensional projections of the same peaks.

X-band Instrumentation—The X-band field sweep and ESEEM measurements were made with an ELEXSYS E580 X-band spectrometer (Bruker, Billerica, MA) with an Oxford CF 935 cryostat.

S-band Instrumentation and Software—The S-band EPR experiments were performed on a home-built pulsed S-band EPR spectrometer (32). Control of the experiment was accomplished through X-epr software using an ELEXSYS console including SpecJet and PatternJet (Bruker BioSpin, Rheinstetten, Germany.) The probe used was an ER 4118CF liquid helium flow cryostat with a Flexline (Bruker) cavity holder and a home-built bridged loop-gap resonator.

Spectral processing of three- and four-pulse ESEEM patterns was performed with Bruker WIN-EPR software. Processing first consisted of subtracting the monotonic component of the decay from time traces (real and imaginary parts) by a cubic or sixth order polynomial to remove the echo decay function. The time trace was then zero-filled to increase the number of experimental data points to a power of one greater than that collected. Following this, a Hamming window function was applied, and the magnitude Fourier spectra were calculated (29–31).

The Factors Leading to the "Cancellation Condition" in ^{14}N ESEEM Spectra—Because of the $I = 1$ nuclear spin, and the quadrupole interactions resulting from this, the ^{14}N nucleus can produce up to six lines in an ESEEM spectrum, three from each of the two electron spin manifolds with $m_S = +½$ or $-½$. In measurements of amorphous (powder) samples (such as the frozen suspensions of the ISF used here), because of their different orientation dependence, not all transitions contribute equally to the spectra. The type of spectrum expected from ^{14}N with predominantly isotropic hyperfine coupling A is governed by the ratio between the effective nuclear frequency in each manifold, $\nu_{ef\pm}$, given by $\nu_{ef\pm} = |\nu_I \pm |A|/2|$, and the quadrupole coupling constant, K, given by $K = e^2qQ/4h$ (23, 24).

If $\nu_{ef\pm}/K = \sim 0$, *i.e.* $\nu_{ef\pm} \cong 0$ (the situation called a cancellation condition because $\nu_I \cong A/2$, *i.e.* the external magnetic field matches the local hyperfine field producing a situation of pure nuclear quadrupole resonance), then the three nuclear frequencies from a corresponding manifold will be close to the three pure nuclear quadrupole resonance (NQR) frequencies of ^{14}N. In this case, three narrow peaks at the following frequencies,

$$\nu_+ = K(3 + \eta) \quad \text{(Eq. 1)}$$

$$\nu_- = K(3 - \eta) \quad \text{(Eq. 2)}$$

$$\nu_0 = 2K\eta \quad \text{(Eq. 3)}$$

would appear in the powder ESEEM spectra, with the property $\nu_+ = \nu_- + \nu_0$ (the term η is an asymmetry parameter). These frequencies would also be present in orientation-selected spectra. However, their intensities depend on the orientation of the magnetic field relative to the g-tensor (*i.e.* cluster) and the respective NQR tensor in each particular experiment. The frequencies described by Equations 1–3. can appear in spectra up to a ratio of $\nu_{ef\pm}/K = \sim 0.75$–1 but are broadened as this value departs from 0.

If $\nu_{ef\pm}/K > 1$, only a single line is expected from each corresponding manifold without any pronounced orientation dependence. This line is produced by a transition at the maximum frequency, which is actually a double-quantum transition between the two outer states with $m_I = -1$ and 1. The frequency of this transition is well described by the following formula,

$$\nu_{dq\pm} = 2[\nu_{ef\pm}^2 + \kappa]^{1/2} \quad \text{(Eq. 4)}$$

where $\kappa = K^2(3 + \eta^2)$. Such a line might show a change in its frequency of the order of $2\Delta(\nu_I)$ that is dependent on orientation selection because of variation of the Zeeman frequency. However, it has an order of ~0.12 MHz in S-band experiments, where the width of the EPR spectrum is ~20 mT.

Two other single-quantum transitions, involving the central level with $m_I = 0$, have a significant orientation dependence from quadrupole interaction and could produce lines at varying frequencies in the orientation-selected spectra.

RESULTS

Two-pulse field sweep X- and S-band electron spin echo spectra of dithionite-reduced Rieske [2Fe-2S] center in ISF show a rhombic EPR line shape consistent with a g-tensor having principal values ($g_{z,y,x} = 2.03, 1.90, 1.76$) (Fig. 1). The width of the EPR line in S-band is smaller than that in X-band and is proportional to the ratio of microwave frequencies used (3.1 GHz for S-band and 9.7 GHz for X-band) (30, 31). In addition, the shape of the field sweep spectrum is influenced by the ESEEM. This influence is different at different regions of the line shape and is stronger in S-band than in X-band. The effect smoothes the g_x feature in the S-band spectrum, which is, however, clearly seen in the X-band spectrum of the same sample.

X-band ^{15}N HYSCORE—X-band ^{15}N HYSCORE spectra measured at different magnetic fields along the EPR line contain the cross-features produced by different types of nitrogens (Fig. 2). In the (+−) quadrant, two pairs of cross-peaks with a contour parallel to the diagonal are detected that have been attributed to the two coordinated $^{15}N_\delta 1,2$ with the hyperfine splittings of the order of 6 and 8 MHz (25). The contour line shape analysis of these features recorded at different field positions (33, 34) gave values for the hyperfine tensors in the axial approximation of $a = 6.6$ and $T = 1.6$ MHz for $N_\delta 1$ and of $a = 7.6$ MHz and $T = 1.5$ MHz for $N_\delta 2$ in ^{15}N-ISF. These tensors are very similar to those reported for other Rieske-type proteins obtained by orientation-selected ^{15}N Q-band electron nuclear double resonance (16) and ^{15}N HYSCORE (25).

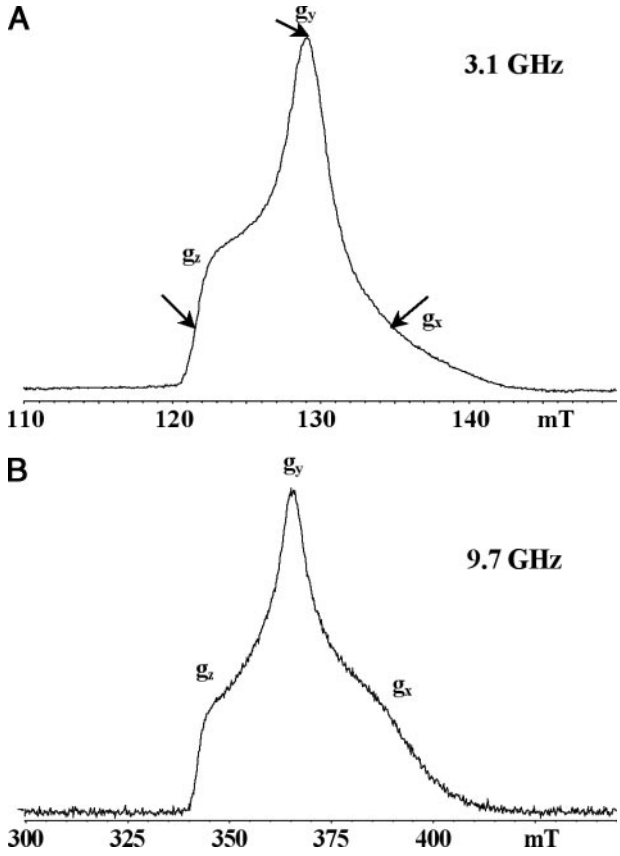

FIGURE 1. **S-band (3.1 GHz) and X-band (9.7 GHz) two-pulse field sweep electron spin echo spectra of the reduced Rieske cluster in the ISF.** The *arrows* mark points on the S-band line shape where the three-pulse spectra shown in Fig. 3 were collected.

Of particular interest in the HYSCORE spectra of ^{15}N-ISF is the (++) quadrant, in which two well resolved pairs of the cross-features are clearly detected at (2.05, 0.95) MHz (N_p) and (1.68, 1.28) MHz (N_ϵ) near g_z. These features are centered symmetrically around the diagonal point with ^{15}N Zeeman frequency and are attributed to weakly coupled ^{15}N in the immediate cluster environment. They were also observed in the HYSCORE spectra recorded near g_x and g_y and also at some intermediate field positions. The splittings are practically the same within the range 1.1–1.2 and 0.3–0.4 MHz in all of the spectra recorded, indicating their predominantly isotropic character. This is a result of the transfer of unpaired spin density onto the corresponding nuclei. Similar couplings were previously observed in the ^{15}N HYSCORE spectra of the archaeal Rieske protein sulredoxin and assigned to the peptide nitrogen of the backbone (larger coupling) and to the remote N_ϵ of coordinating histidine ligands (smaller coupling) (25). From these results, we can tentatively suggest the same assignment for ISF. However, neither ISF nor sulredoxin show spectra that resolve two different couplings from N_ϵ-atoms, probably because of the small differences between them.

S-band ESEEM and HYSCORE—Although the ^{15}N HYSCORE spectra at X-band provide evidence for the presence of weakly coupled nitrogens, we could only speculate about their chemical nature. To obtain additional information about these nitrogens, we have employed S-band ESEEM spectroscopy.

Fig. 3 shows typical three-pulse S-band ESEEM spectra of ISF with natural isotope abundance in the region appropriate for the ^{14}N nuclei, recorded at three different magnetic fields that select the principal values of the g-tensor (Fig. 1). Comparison of the spectra shows that a complete set of frequencies appeared at all three fields, including peaks at 0.6, 1.5, 1.8, 2.3, 2.9, and 3.4 MHz. These frequencies were also seen along the diagonal of the HYSCORE spectra. One can note with high accuracy, that the frequencies from the set that are observed in at least two spectra (0.6, 1.5, 2.3, and 2.9 MHz) are independent of the applied magnetic field and the excitation point within the EPR spectrum. Additional information about relative relations between these frequencies was obtained from the S-band HYSCORE spectra. The spectrum recorded at 129 mT (near g_y) showed cross-peaks at (1.5, 1.8) MHz, indicating that these frequencies belong to two opposite electron spin manifolds of the same nucleus.

DISCUSSION

We have taken advantage of two features of nitrogen nuclear spin systems to examine the properties of atoms interacting weakly with the electron spin of the [2Fe-2S] cluster. The first of these relates to the different energy levels (frequencies) from quadrupolar spin interactions of the ^{14}N nucleus and the different magnetic fields needed to achieve the optimal conditions for its observation with reference to the Zeeman frequency on switching between X-band and S-band (see discussion of the cancellation condition under "Experimental Procedures"). The second arises from the simplification in spectra when dealing with the $I = ½$ ^{15}N nucleus compared with the $I = 1$ ^{14}N nucleus, because the former lack the quadrupolar features of the latter.

X-band Versus S-band—The lines observed in S-band ^{14}N ESEEM spectra of the Rieske cluster appear at different fields from those seen in ^{14}N X-band spectra, because the resonance condition depends on field strength. Previous studies of the Rieske cluster in different proteins by X-band one- and two-dimensional ESEEM (20–22) have shown that the major contributions in these spectra come from the coordinating N_δ of histidines with hyperfine couplings of the order of 4–5 MHz. The dominating features of X-band ESEEM spectra of ISF are similar to the spectra of other Rieske clusters and result from two N_δ atoms. The weakly coupled nitrogens do not produce readily recognizable lines in ^{14}N X-band spectra; this simplifying feature aids unambiguous assignment but at the expense of further information. However, their contribution is clearly seen in the ^{15}N spectra, together with the peaks from N_δ as shown above (Fig. 2).

The basic parameter distinguishing between X-band and S-band ESEEM spectra is the difference in field strength needed to obtain resonance, which leads to a different value for the Zeeman frequency. It is about three times smaller in S-band (~0.37–0.42 MHz) than in X-band (~1.05–1.1 MHz). The hyperfine couplings of the coordinated N_δ exceed the Zeeman frequency by a factor of 4–5 in X-band. Usually the ^{14}N nuclei produce well resolved and intense ESEEM spectra under such conditions. However, any further increase of the couplings relative to the Zeeman frequency leads to the suppression of the

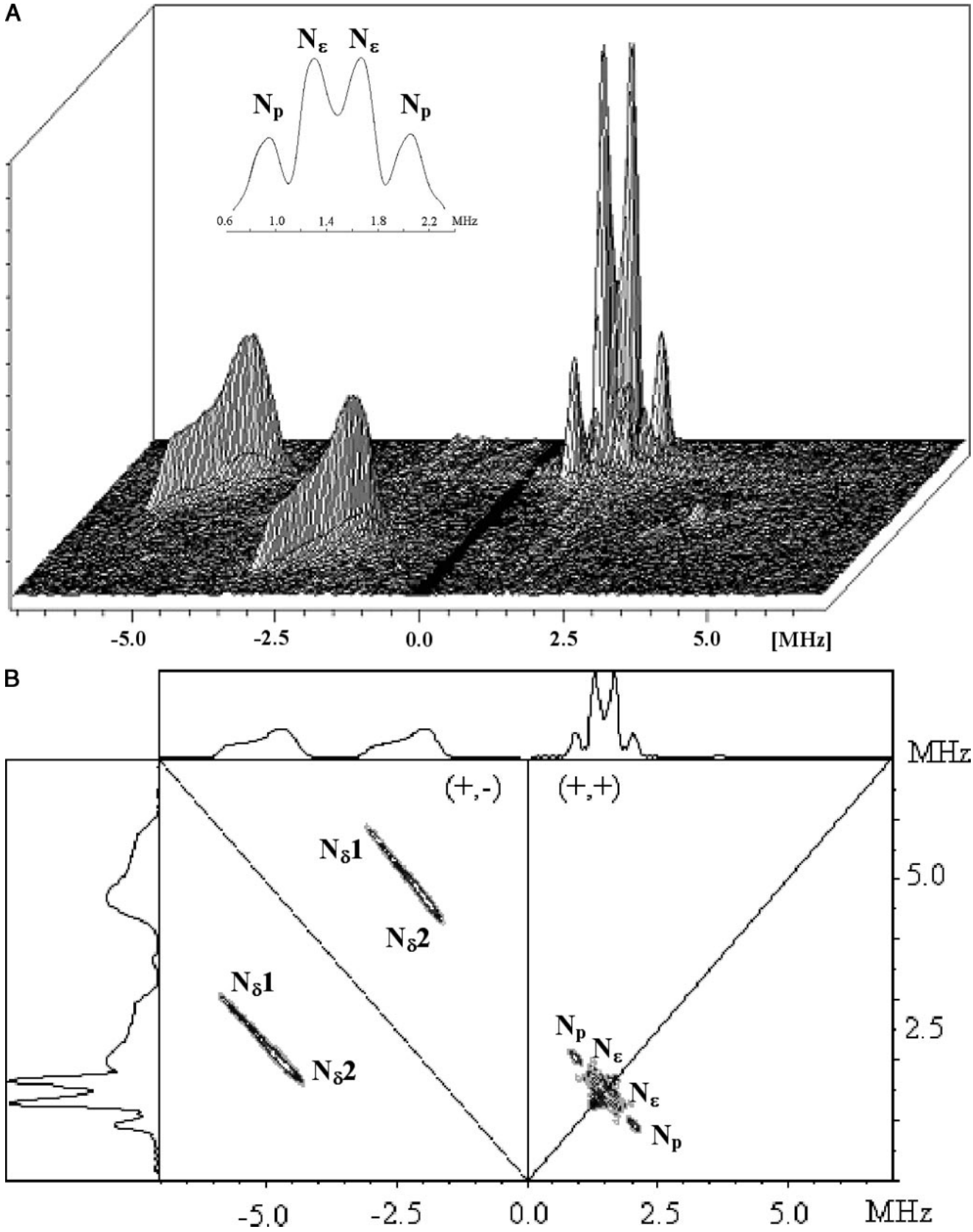

FIGURE 2. **The three-dimensional presentations (*top panel*) and the contour plots (*bottom panel*) of ^{15}N-HYSCORE spectrum of the reduced Rieske cluster in the ^{15}N-labeled ISF.** The data were recorded near $g_z = 2.01$; magnetic field, 342.5 mT; $\tau = 136$ ns; microwave frequency, ~9.70 GHz; temperature, 10 K. The cross-peaks from the strongly and weakly coupled ^{15}N nuclei are located in the $(+-)$ and $(++)$ quadrants, respectively. The insert in the three-dimensional presentation shows the sky-line projection along the line crossing the diagonal of the $(++)$ quadrant at the point with both coordinates equal to ^{15}N Zeeman frequency.

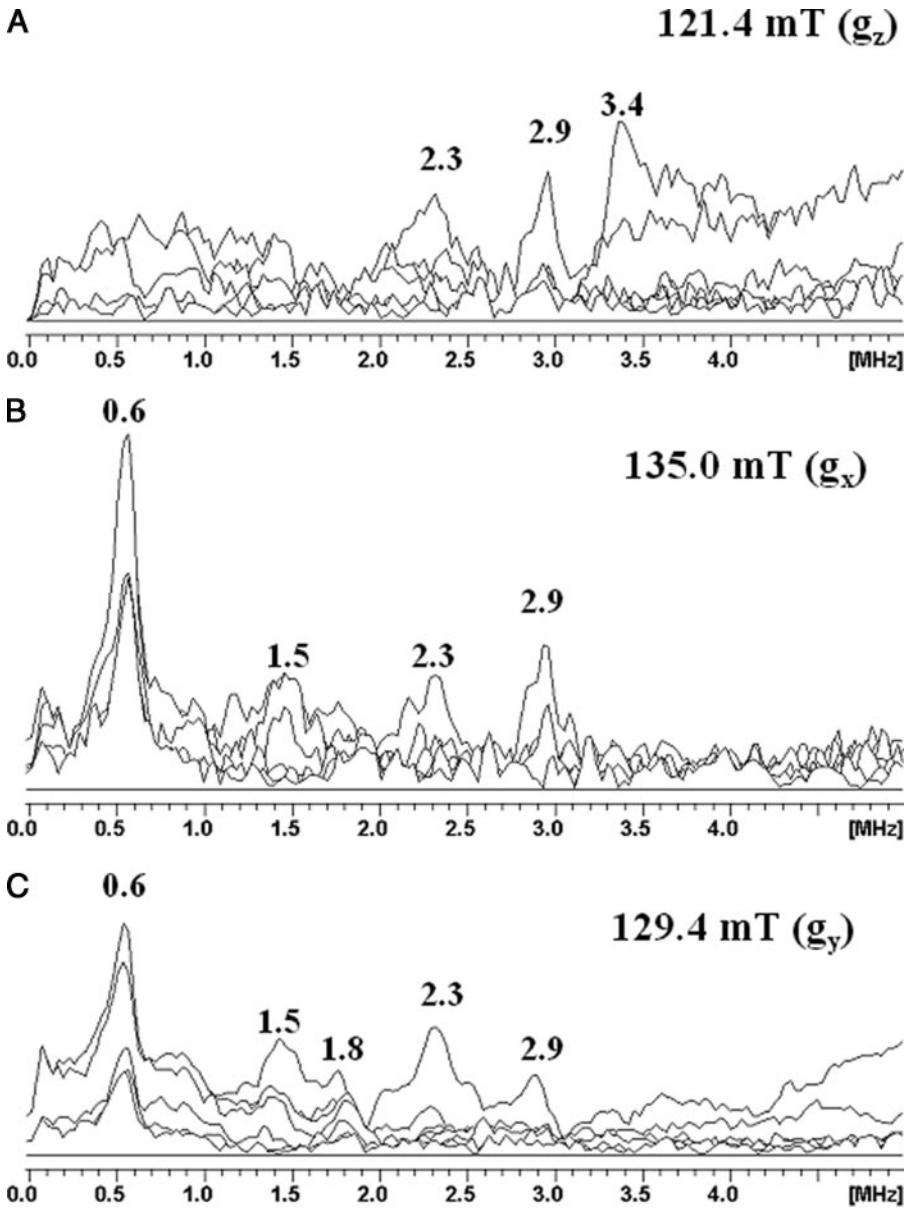

FIGURE 3. **Stacked plots of S-band three-pulse ESEEM spectra after modulus Fourier transformation along time T between the second and third microwave pulses for the reduced Rieske cluster in the ISF.** The spectra were measured near g_z (121.4 mT), g_y (129.4 mT), and g_x (135.0 mT) (Fig. 1). The spectra are plotted from the back (corresponding to an initial time, $\tau = 184$ ns) to the front, and successive spectra are obtained by increasing τ in steps of 30 ns.

TABLE 1

The contribution of strongly and weakly coupled nitrogens to ^{14}N ESEEM spectra

Band	N_δ	N_p,N_ϵ
X-band	Strong lines	Unclear
S-band	Not seen	Well resolved

spectral intensity (23). The ratio of hyperfine couplings and the Zeeman frequency is increased from 4–5 to 12–15 in S-band, and the spectral lines from N_δ have a negligible intensity, *i.e.* they are not observed in the spectra (Table 1). On the other hand, the ^{14}N Zeeman frequency in X-band exceeds the couplings (0.7 and 0.25 MHz recalculated from ^{15}N couplings) from weakly coupled N_p and N_ϵ, whereas in S-band the Zeeman frequency is smaller or comparable with these couplings. At this scale, the powder spectra observed for ^{14}N ESEEM also depend on the value of the quadrupole coupling constant.

Assignment of the Frequencies in S-band Spectra—Lines with stable frequencies observed in at least two S-band spectra recorded at different positions along the EPR line are likely to be close to the pure NQR frequencies of nitrogens or their double-quantum transitions.

Previous data have indicated that the protonated N_ϵ-H of the imidazole ring possesses a stable (quadrupole) coupling constant of $K = 0.35$ MHz and a high asymmetry parameter $\eta = 0.915–0.995$ in noncoordinated imidazole and histidine (35–37). Only slight variations of the quadrupole coupling constant ($K = 0.35–0.43$ MHz) have been demonstrated for the amine N_ϵ nitrogen in metal complexes of imidazole coordinated via N_δ nitrogen (38–41). One might therefore expect a set of NQR lines from N_ϵ in the range 1.4–1.6 MHz for ν_+ and 0.7–0.8 MHz for ν_- and ν_0.

The hyperfine coupling 0.3–0.4 MHz tentatively assigned above to the N_ϵ from the ^{15}N HYSCORE is equivalent to 0.25 ± 0.03 MHz when recalculated to ^{14}N. This gives $\nu_{ef-} = 0.28$ MHz for $\nu_I = 0.4$ MHz, and defines the ratio $\nu_{ef-}/K = 0.65–0.8$ for $K = 0.35–0.43$ MHz. This ratio is quite high, at the borderline of the cancellation condition. We do not therefore expect all peaks to show the narrow lines close to pure quadrupole frequencies of ^{14}N as anticipated under cancellation conditions (23). Nevertheless, simulations show that the highest NQR line ($\nu_+ = \sim 1.4–1.6$ MHz in the case of N_ϵ) would retain its narrow shape as the ν_{ef-}/K ratio deviates from the cancellation condition (42). The line at 1.5 MHz observed in the S-band spectra (Fig. 3) can therefore be assigned to this highest frequency, which comes from the manifold with $\nu_{ef-} = |\nu_I - |A|/2|$ of the protonated N_ϵ-atoms, with hyperfine coupling at ~0.25 MHz.

From the above, one can calculate the frequency of the formal double-quantum transition (Equation 4) from the opposite manifold with $\nu_{ef+} = |\nu_I + |A|/2| = 0.65$ MHz and $\nu_{ef+}/K = 1.5–1.9$. This gives an estimate of 1.76–1.9 MHz for $K = \sim 0.4$ MHz and η varying between 0 and 1. This value is consistent with the frequency 1.8 MHz observed in the three-pulse spectra

of Fig. 3, which is involved in cross-correlation with the frequency 1.5 MHz in the HYSCORE spectrum.

The exact cancellation condition, $\nu_{ef-} = |\nu_I - |A/2|| \sim 0$, is well approximated in the S-band experiment for the ^{14}N (Fig. 3), with the second hyperfine coupling $A = \sim 0.7$ MHz determined from the X-band HYSCORE experiment of Fig. 2. Three frequencies, at 0.6, 2.3, and 2.9 MHz, which are also observed in the S-band spectra, satisfy the condition for the NQR frequencies, *i.e.* the sum of the two lower frequencies is equal to the maximum frequency. These three frequencies allow one to determine $K = 0.87$ MHz and $\eta = 0.34$. The value of the quadrupole coupling constant K is close to the typical values $\sim$0.75–0.85 MHz previously reported for peptide nitrogens (43–47). Calculation of the double-quantum transition for this nitrogen, with $A = 0.7$ MHz and the nuclear quadrupole interaction parameters found, gives a value 3.4 MHz, consistent with the frequency observed in three-pulse S-band spectrum at g_z (Fig. 3).

Thus, the S-band ^{14}N ESEEM spectra of the Rieske cluster in ISF could best be explained as a superposition of the lines from two types of nitrogens, with quadrupole couplings typical of an imidazole amine nitrogen, N_ϵ, and of amide peptide nitrogen, N_p, with the hyperfine couplings determined from ^{15}N HYSCORE spectra. This result directly defines the weakly coupled nitrogens as N_ϵ and N_p, in agreement with our previous tentative assignments (25).

Spin Density on the N_ϵ—The intense pair of cross-features with smaller splittings of 0.3–0.4 MHz seen in spectra of ^{15}N-ISF belong to N_ϵ-atoms of the histidyl ligands. The literature values for isotropic hyperfine couplings for coordinated N_δ and remote N_ϵ of the imidazole rings ligated to Cu(II) and VO(II) in various model complexes and in proteins of well defined structure have an almost constant ratio of about 20 between the N_δ and N_ϵ couplings (although both couplings in the Cu(II) complexes are much larger than those in the VO(II) complexes) (48, 49). The couplings of $\sim$6–8 MHz for the two N_δ-atoms coordinated to the Rieske-type [2Fe-2S] clusters are very close to those of the N_δ equatorially coordinated to the VO(II) complexes (49), and the N_ϵ nuclei in the latter compounds show coupling in the range of 0.3–0.4 MHz, as observed in the present HYSCORE spectra of ^{15}N-ISF (Fig. 2) and other Rieske proteins (25). Thus, the ratio $\sim$20 between hyperfine couplings of the N_δ and N_ϵ applies to the coordinated imidazoles in the Rieske cluster. This stability probably reflects the analogous mechanism of spin density transfer from the metal over the imidazole ring to the N_ϵ, which is also sensitive to protonation state (34). In view of this result, it would be interesting to study the N_ϵ hyperfine couplings for the Rieske cluster in the bc_1 complex to explore the interaction of ISP with occupants of the Q_o site via the H-bond with the N_ϵ-H of one of the histidine ligands.

Identification of the Peptide Nitrogen—Comparison of the intensities of the lines in the S-band ESEEM spectra assigned to the NQR frequencies of the peptide nitrogen recorded at different points along the EPR line makes it possible to identify a particular peptide nitrogen that carries the maximum unpaired spin density from among all of the peptide nitrogens around the Rieske cluster (48).

The amide nitrogen in free peptides, such as in metal complexes of diglycine, which H-bond to the inorganic sulfur atoms of iron-sulfur clusters (43–48), has a narrow range of quadrupole coupling constants, $K = 0.75$–0.85 MHz, determined by the electronic structure and the geometry of the planar peptide group. This coupling constant is only slightly perturbed by hydrogen bonding, which has been confirmed by calculations of the quadrupole coupling tensor (46, 50, 51). Calculations based on the isolated molecules yield quadrupole coupling tensors for the peptide nitrogen very close to experimental values, confirming the negligible influence of hydrogen bonding. From these calculations, the maximum principal value is normal to the local peptide plane; the intermediate element almost coincides with the C(O)-N(H) bond, and the minimal element points about 30° from the N–H-bond.

A significant increase in the intensity of the lowest NQR line, ν_0, at 0.6 MHz is clearly seen from the three-pulse ESEEM spectra (Fig. 3) when the magnetic field is applied close to the g_x principal value of the Rieske cluster. Theoretical considerations (23, 52) indicate that the increase of ν_0 intensity occurs when both vectors B_o and g_x closely coincide with the axis of maximal principal value of the NQR tensor.

To interpret the magnetic resonance data in conjunction with crystal structures, one needs to know the orientation of the g-tensor principal axes. Recently, a single-crystal EPR study of the reduced Rieske cluster in cytochrome bc_1 complex with stigmatellin, showed that the g_z, g_x, and g_y axes are not oriented exactly along the sulfur-sulfur and iron-iron directions and nearly normal to the cluster plane of the cluster, respectively, as theoretically predicted (53). The g-tensor principal axes are skewed with respect to the iron-iron and sulfur-sulfur atom direction in the [2Fe-2S] cluster. For instance, the $g_x \sim 1.79$ axis makes an average angle of 30° with respect to the Fe-Fe direction and the $g_z \sim 2.024$ axis an average angle of 26° with respect to the sulfur-sulfur direction.

We have used the available x-ray structure of the ISF from *R. sphaeroides* (Fig. 4) to characterize the orientation of the peptide plane and the normal to this plane for the peptide nitrogens located within 5 Å around Rieske cluster.[5] The orientation of the g_x principal axis in the same coordinate system was determined using the single-crystal EPR data of Bowman *et al.* (53). This information has allowed us to calculate the angles between the axis of the maximum principal value of the NQR tensor (*i.e.* normal to the peptide plane determined by the location of N- and C=O-atoms) for different peptide nitrogens, and g_x principal direction of the g-tensor. These calculations (Table 2) have found that the minimum angle between these two axes belongs to the peptide nitrogen from Leu-132. This angle in the intact bc_1 complex is equal to 6° for monomer A (*i.e.* deviation from coincidence of two directions is very small) and increased up to 24° for monomer B, with an average value of 15°. All of the other angles significantly exceed this angle and thus would not satisfy the observed variations caused by orientation in ESEEM spectra.

[5] D. R. Kolling, J. S. Brunzelle, S. Lhee, A. R. Crofts, and S. K. Nair, submitted for publication.

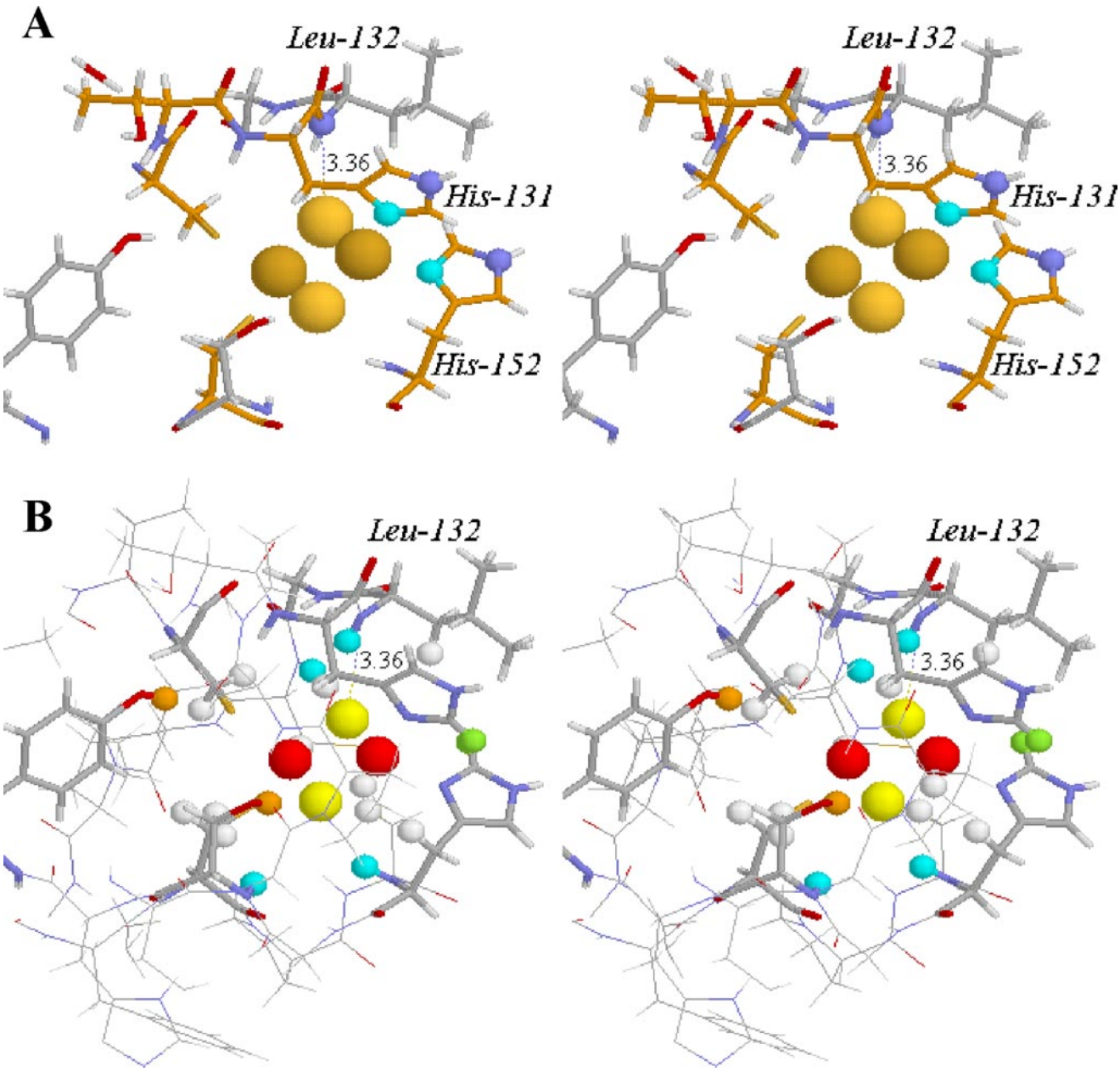

FIGURE 4. **The structure of the ISF from *R. sphaeroides* at 1.2 Å,[5] showing features discussed in the text.** *A*, N-atoms to which spin density can be assigned: residues near the [2Fe-2S] cluster (larger spheres in CPK coloring) are shown as stick models. The N-atoms identified by ESEEM are shown as smaller spheres colored *cyan* (N_δ of His-131, His-152) or *blue* (N_ϵ of His-131, His-152, or N-backbone of Leu-132). *B*, H-atoms in the cluster environment: 18 protons within 3.5 Å are shown, of which HYSCORE ^{1}H spectroscopy can distinguish at least 10, three of which are exchangeable (D. R. J. Kolling, R. I. Samoilova, A. R. Crofts, and S. A. Dikanov, unpublished observations). The [2Fe-2S] cluster is shown as larger spheres colored *red* (iron) and *yellow* (sulfur). H-atoms are smaller spheres, colored *white* (methyl(ene)), *cyan* (>NH), *orange* (-OH), or *green* (His >CH). Important residues are shown as stick models. Other atoms within 10.0 Å are in wire frame. Leu-132 is labeled, and the H-bond distance from the peptide N to cluster S2 is shown. Both images are stereo views for crossed-eye viewing.

TABLE 2

Angles between the g_x axis of the g-tensor and the axis of maximum principal value of the NQR tensor of peptide nitrogens

Nitrogen	θ°		Average angle	N-H–S distance
	Chain A	Chain B		
				Å
N1377 Cys-134	54.0	38.3	46	3.69
N1370 Gly-133	95.5	92.5	94	3.78
N1351 Leu-132	6.5	24.0	15	3.36
N1611 His-152	60.2	62.3	61	3.42
N1629 Gly-153	104.9	109.6	107	3.80
N1636 Ser-154	45.8	36.1	41	3.71

One can conclude that the peptide nitrogen possessing the highest unpaired spin density is that of Leu-132. Although the -N-H–S2 distance of 3.36 Å is relatively long, the spin density observed shows that this nitrogen is involved in hydrogen bond formation with the cluster, with a favorable path for the spin density transfer. Peptide nitrogens from the other 5 residues located within H-bond distance of the ISP cluster carry at least 5–10 times less spin density and give neither resolved splittings in the spectra of ^{15}N-labeled protein nor intensive narrow lines from the ^{14}N nuclei in the

TABLE 3
The ϕ and ψ torsional angles for the protein backbone in the span LGCV obtained from high resolution structures (all angles are in degrees)

Source	ϕ	ψ	ϕ	ψ	ϕ	ψ	ϕ	ψ	Ref.
Mitochondrial	**Leu-142**		**Gly-143**		**Cys-144**		**Val-145**		
Bovine	−130.3	18.7	91.1	2.3	−69.4	178.7	−100	119	19
Chloroplast	**Leu-110**		**Gly-111**		**Cys-112**		**Val-113**		
Spinach	−126.7	6.2	91.3	15.7	−73.6	159	−87.3	121	54
R. sphaeroides	**Leu-132**		**Gly-133**		**Cys-134**		**Val-135**		
Wild type	−132.2	18.1	89.9	9.4	−64.1	163.8	−88.3	143.2	[a]
G133S	−140.7	179.7	−76.4	107	−161.1	144.3	−97.5	114.2	[b]

[a] D. R. Kolling, J. S. Brunzelle, S. Lhee, A. R. Crofts, and S. K. Nair, submitted for publication.
[b] S. Lhee, D. R. J. Kolling, A. R. Crofts, and S. K. Nair, manuscript in preparation.

native protein. One can note however, that the line shape of the central doublet caused by splitting by the $^{15}N_{\epsilon}$ (Fig. 2) is not identical in different Rieske proteins. We therefore cannot exclude some small additional nonequivalent unresolved contribution from other weakly coupled nitrogens to this line. The differences observed could be attributed to other variations in the H-bond network in different proteins.

A similar coupling of ~1.1–1.5 MHz (for ^{15}N) has been observed in the spectra of other Rieske proteins (high potential sulredoxin (25) and a low potential archaeal Rieske ferredoxin), and in classical ferredoxins,[6] which may indicate the presence of a similar hydrogen bond transferring an excess of unpaired spin density onto the peptide nitrogen. If so, this configuration might be a common motif, not linked specifically to the differences in cluster potential, but a structural component of all [2Fe-2S] clusters. Additional support for this view comes from NMR experiments with the Rieske-ferredoxin component of toluene-4-monooxygenase (55), selectively labeled with ^{15}N on specific residues. The NMR spectra show that the peptide nitrogen of Gln-48 (the analogue of Leu-132 in ISF) in the reduced protein possesses a hyperfine-shifted resonance with maximal chemical shift of ~426 ppm. This nitrogen also undergoes the largest change of chemical shift (~300 ppm) on reduction of the Rieske cluster. This large change is probably due to a contribution of contact shift, resulting from the appearance of a large unpaired spin density on its nucleus.

Mechanistic Implications—Detailed density function theory/electrostatic calculations have been able to account for the redox and p*K* value differences between strains in terms of H-bonding and local negative charge from side chains substitutions (56–58). Because the H-bond donor in Leu-132 is a backbone N-H, mutagenesis cannot be used to test its role. The backbone configuration of the loop following the first pair of ligands (the conserved sequence ***C***T***H***LGCVP, where the ligands are in bold italic) is determined by residues Leu-132, Gly-133, and Cys-134 (residues 142–144 in the beef or chicken complexes), which are conserved in the Rieske proteins from all α-proteobacterial bc_1 complexes. Each of these residues has an interesting structural role. In the mechanism of QH_2 oxidation in the intact complex, Leu-132 provides a contact with the *b*-interface at which the ISP mobile domain is docked on cytochrome *b*. The interface is tightly packed, and this strongly constrains the configuration. It also constrains the possibilities for mutational analysis. Residues tolerated at this position in *R. sphaeroides* include alanine and tyrosine,[7] but function is impaired, indicating that the constrained configuration in the wild type is important for optimal turnover. Other mutations have been explored through recombinant expression of the bovine protein in *Escherichia coli* and show relatively weak variation in thermodynamic characteristics but substantial changes in EPR spectra (59). However, structures are not yet available for any of these proteins. A wider range of substitutions is tolerated at Gly-133, but any substitution gives rise to some impairment of function. The explanation is immediately apparent on examination of the ϕ and ψ torsional angles for this (or the equivalent) span in solved structures (Table 3). Those for this glycine occupy a region of the Ramachandra space accessible only to glycine, so that any substitution will force a reorientation of the backbone. Although this site was among those generated as spontaneous mutations in earlier studies, detailed mutagenic analysis has been limited (8, 9, 60, 61). In work currently in progress, we have constructed a range of mutants and are currently characterizing these. For one strain, G133S, the crystallographic structure has been solved at ~1.5 Å resolution, and the ϕ and ψ torsional angles for this strain are included in Table 3. The reconfiguration of the backbone orientation results in a substantial change in local dipole orientations, so that the -C=$O^{\delta-}$ points toward the cluster, and the -N-$H^{\delta+}$ points away, which is the reverse of the wild type. This dipolar reorientation would likely contribute to a change in thermodynamic properties, but the extent of this is currently under investigation using the wider set of mutant strains. The reconfiguration of the backbone does not propagate far; on the N-side, the -N-H-S_2 distance for Leu-132 is changed by only 0.05 Å (3.41 instead of 3.36 Å), and the backbone configuration is not changed beyond the next residue, Cys-144. This is involved in a conserved disulfide linkage that stabilizes the loop, and the side chain and sulfur-sulfur bond have the same position in wild type and G133S mutant. The disulfide linkage appears to have little effect in redox properties (59). From this discussion, it will be apparent that the structural information currently available and results from mutagenesis favor a nonspecific role for the H-bond from Leu-132 -NH to S_2 and that further exploration of this span through mutagenesis will likely

[6] T. Iwasaki and S. A. Dikanov, unpublished observations.

[7] S. Lhee and A. R. Crofts, unpublished observations.

be most informative in the context of the Leu-132 and Gly-133 mutants currently under study.

REFERENCES

1. Mason, J. R., and Cammack, R. (1992) *Annu. Rev. Microbiol.* **46,** 277–305
2. Trumpower, B. L., and Gennis R. B. (1994) *Annu. Rev. Biochem.* **63,** 675–716
3. Link, T. A. (1999) *Adv. Inorg. Chem.* **47,** 83–157
4. Berry, E. A., Guergova-Kuras, M., Huang, L.-S., and Crofts, A. R. (2000) *Annu. Rev. Biochem.* **69,** 1005–1075
5. Crofts, A. R. (2004) *Annu. Rev. Physiol.* **66,** 689–733
6. Crofts, A. R. (2004) *Biochim. Biophys. Acta* **1655,** 77–92
7. Hong, S. J., Ugulava, N., Guergova-Kuras, M., and Crofts, A. R. (1999) *J. Biol. Chem.* **274,** 33931–33944
8. Gatti, D. L., Meinhardt, S. W., Ohnishi, T., and Tzagoloff, A. (1989) *J. Mol. Biol.* **205,** 421–435
9. Van Doren, S. R., Gennis, R. B., Barquera, B., and Crofts, A. R. (1993) *Biochemistry* **32,** 8083–8091
10. Denke, E., Merbitzzahradnik, T., Hatzfeld, O. M., Snyder, C. H., Link, T. A., and Trumpower, B. L. (1998) *J. Biol. Chem.* **273,** 9085–9093
11. Schröter, T., Hatzfeld, O. M., Gemeinhardt, S., Korn, M., Friedrich, T., Ludwig, B., and Link, T. (1998) *Eur. J. Biochem.* **255,** 100–106
12. Snyder, C., and Trumpower, B. L. (1998) *Biochim. Biophys. Acta* **1365,** 125–134
13. Guergova-Kuras, M., Kuras, R., Ugulava, N., Hadad, I., and Crofts, A. R. (2000) *Biochemistry* **39,** 7436–7444
14. Gurbiel, R. J., Batie, C. J., Sivaraja, M., True, A. E., Fee, J. A., Hoffman, B. M., and Ballou, D. P. (1989) *Biochemistry* **28,** 4861–4871
15. Gurbiel, R. J., Ohnishi, T., Robertson, D. E., Daldal, F., and Hoffman, B. M. (1991) *Biochemistry* **30,** 11579–11584
16. Gurbiel, R. J., Doan, P. E., Gassner, G. T., Macke, T. J., Case, D. A., Ohnishi, T., Fee J. A., Ballou, D. P., and Hoffman, B. M. (1996) *Biochemistry* **35,** 7834–7845
17. Britt, R. D., Sauer, K., Klein, M. P., Knaff, D. B., Kriauciunas, A., Yu, C. A., Yu, L., and Malkin, R. (1991) *Biochemistry* **30,** 1892–1901
18. Shergill, J. K., and Cammack, R. (1994) *Biochim. Biophys. Acta* **1185,** 35–42
19. Iwata, S., Saynovits, M., Link, T. A., and Michel, H. (1996) *Structure* **4,** 567–579
20. Shergill, J. K., Joannou, C. L., Mason, J. R., and Cammack, R. (1995) *Biochemistry* **34,** 16533–16542
21. Dikanov, S. A., Xun, L., Karpiel, A. B., Tyryshkin, A. M., and Bowman, M. K. (1996) *J. Am. Chem. Soc.* **118,** 8408–8416
22. Dikanov, S. A., Shubin, A. A., Kounosu, A., Iwasaki, T., and Samoilova, R. I. (2004) *J. Biol. Inorg. Chem.* **9,** 753–767
23. Flanagan, H., and Singel, D. J. (1987) *J. Chem. Phys.* **87,** 5606–5616
24. Dikanov, S. A., Tsvetkov, Yu. D., Bowman, M. K., and Astashkin, A. V. (1982) *Chem. Phys. Lett.* **90,** 149–153
25. Iwasaki, T., Kounisu, A., Uzawa, T., Samoilova, R. I., and Dikanov, S. A. (2004) *J. Am. Chem. Soc.* **125,** 13902–13903
26. Guergova-Kuras, M., Salcedo-Hernandez, R., Bechmann, G., Kuras, R., Gennis, R. B., and Crofts, A. R. (1998) *Protein Expression Purif.* **15,** 370–380
27. Iwasaki, T., Kounosu, A., Kolling, D. R. J., Crofts, A. R., Dikanov, S. A., Jin, A., Imai, T., and Urushiyama, A. (2004) *J. Am. Chem. Soc.* **126,** 4788–4789
28. Iwasaki, T., Kounosu., A., Kolling, D. R. J., Lhee, S., Crofts, A. R., Dikanov, S. A., Uchiyama, T., Kumasaka, T., Ichikawa, H., Kono M., Imai., T., and Urushiyama, A. (2006) *Protein Sci.* **15,** 2019–2024
29. Dikanov, S. A., and Tsvetkov, Yu. D. (1992) *Electron Spin Echo Envelope Modulation (ESEEM) Spectroscopy*, p. 412, CRC Press, Boca Raton, FL
30. Schweiger, A., and Jeschke, G. (2001) *Principles of Pulse Electron Paramagnetic Resonance*, p. 578, Oxford University Press, Oxford, UK
31. Weil, J. A., Bolton, J. R., and Wertz, J. E. (1994) *Electron Paramagnetic Resonance: Elementary Theory and Applications*, p. 308, Wiley Interscience, New York
32. Weber, A., Rohrer, M., Törring, J. T., and Prisner, T. F. (1998) in *Proceedings of the 29th Congress AMPERE/13th ISMAR* (Ziessow, D., Lubitz, W., and Lendzian, F., eds) Vol. 2, p. 1138, International Society of Magnetic Resonance, Berlin, August 2–7, 1998
33. Dikanov, S. A., and Bowman, M. K. (1998) *J. Biol. Inorg. Chem.* **3,** 18–29
34. Iwasaki, T., Kounosu, K., Samoilova, R. I., and Dikanov, S. A. (2006) *J. Am. Chem. Soc.* **128,** 2170–2171
35. Edmonds, D. T., and Summers, C. P. (1973) *J. Magn. Reson.* **12,** 134–142
36. Hunt, M. J., Mackay, A. L., and Edmonds, D. T. (1975) *Chem. Phys. Lett.* **34,** 473–475
37. Hunt, M. J., and Mackay, A. L. (1976) *J. Magn. Reson.* **22,** 295–301
38. Ashby, C. I. H., Cheng, C. P., and Brown, T. L. (1978) *J. Am. Chem. Soc.* **100,** 6057–6063
39. Mims, W. B., and Peisach, J. (1978) *J. Chem. Phys.* **69,** 4921–4930
40. Jang, F., McCracken, J., and Peisach, J. (1990) *J. Am. Chem. Soc.* **112,** 9035–9044
41. Colaneri, J., and Peisach, J. (1992) *J. Am. Chem. Soc.* **114,** 5335–5341
42. Reijerse, E. J., and Keijzers, C. P. (1987) *J. Magn. Reson.* **71,** 83–96
43. Edmonds, D. T., and Speight, P. A. (1971) *Phys. Lett. A* **34,** 325–326
44. Blinc, R., Mali, M., Osredkar, R., Seliger, J., and Ehrenberg, L. (1974) *Chem. Phys. Lett.* **28,** 158–159
45. Ashby, C. I., Paton, W. F., and Brown, T. L. (1980) *J. Am. Chem. Soc.* **102,** 2990–2998
46. Rabbani, S. R., Edmonds, D. T., Gosling, P., and Palmer, M. H. (1987) *J. Magn. Reson.* **72,** 230–237
47. Dikanov, S. A., Tyryshkin, A. M., Felli, I., Reijerse, E. J., and Hüttermann, J. (1995) *J. Magn. Reson. B* **108,** 99–102
48. Mims, W. B., and Peisach, J. (1989) in *Advanced EPR: Applications in Biology and Biochemistry* (Hoff, A. J., ed) pp. 1–57, Elsevier Science Publishers B.V., Amsterdam
49. Dikanov, S. A., Samoilova, R. I., Smieja, J. A., and Bowman, M. K. (1995) *J. Am. Chem. Soc.* **117,** 10579–10580
50. Palmer, M. H. (1984) *Z. Naturforsch. A* **39,** 1108–1111
51. Elmi, F., and Hadipour, N. L. (2005) *J. Phys. Chem. A* **109,** 1729–1733
52. Benetis, N. P., and Dikanov, S. A. (2005) *J. Magn. Reson.* **175,** 124–145
53. Bowman, M. K., Berry, E. A., Roberts, A. G., and Kramer, D. M. (2004) *Biochemistry* **43,** 430–436
54. Carrell, C. J., Zhang, H., Cramer, W. A., and Smith, J. L. (1997) *Structure* **5,** 1613–1625
55. Xia, B., Pikus, J. D., Xia, W., McClay, K., Steffan, R. J., Chae, Y. K., Westler, W. M., Markley, J. L., and Fox, B. G. (1999) *Biochemistry* **38,** 727–739
56. Ullmann, G. M., Noodleman, L., and Case, D. A. (2002) *J. Biol. Inorg. Chem.* **7,** 632–639
57. Klingen, A. R., and Ullmann, G. M. (2004) *Biochemistry* **43,** 12384–12389
58. Li, J., Nelson, M. R., Peng, C. Y., Bashford, D., and Noodleman, L. (1998) *J. Phys. Chem. A Mol. Spectrosc. Kinet. Environ. Gen. Theory* **102,** 6311–6324
59. Leggate, E. J., and Hirst, J. (2005) *Biochemistry* **44,** 7048–7058
60. Davidson, E., Ohnishi, T., Atta-Asafo-Adjei, E., and Daldal, F. (1992) *Biochemistry* **31,** 3342–3351
61. Davidson, E., Ohnishi, T., Tokito, M., and Daldal, F. (1992) *Biochemistry* **31,** 3351–3358